Combustion and Flame 159 (2012) 2077–2086

Contents lists available at SciVerse ScienceDirect

Combustion and Flame

journal homepage: www.elsevier.com/locate/combustflame

The propagation of a laminar reaction front during end-gas auto-ignition

Jason B. Martz *, George A. Lavoie, Hong G. Im, Robert J. Middleton, Aristotelis Babajimopoulos, Dionissios N. Assanis

Mechanical Engineering Department, University of Michigan, Ann Arbor, MI 48109, United States

ARTICLE INFO

Article history:
Received 22 January 2011
Received in revised form 20 October 2011
Accepted 15 January 2012
Available online 3 March 2012

Keywords:
Auto-ignition
Knock
Laminar burning velocity
Low temperature combustion
Spark assisted compression ignition
Spark ignition

ABSTRACT

A transient, one dimensional premixed laminar reaction front is used as a model problem to further understand the physical processes influencing reaction front propagation during the various stages of spark-assisted compression ignition (SACI) combustion for both constant and variable domain pressures. This approach is consistent with the wrinkled laminar flame representation of turbulent, spark ignited engine combustion. With the proper choice of timescales and pressure rise rate, it applies to the interaction of the flame with auto-igniting end-gas in a typical automotive engine. Under the conditions simulated by a transient flame code, the reaction front begins as a deflagration, propagating into an end-gas with an initially negligible level of reaction progress. The diffusive–reactive nature of the front is maintained until significant levels of end-gas reaction progress, where the burning velocity depends upon the degree of pre-reaction. At the time of the end-gas maximum chemical power, the maximum temperature gradient and peak rate of heat conduction within the front diminish to the point where combustion becomes chemically controlled. Although significant increases in burning velocity are observed at the onset of chemically controlled combustion within the front, the end-gas is within one front time from the completion of combustion. As a result, no more than one front thickness is consumed by the apparent propagation of the spontaneous ignition front.

1. Introduction

While engine systems operating with homogeneous charge compression ignition (HCCI) combustion are capable of elevated thermal efficiency and low emissions, the implementation of HCCI remains challenging because it lacks a direct control mechanism for the phasing of combustion [1]. Recent studies on spark-assisted compression ignition (SACI) combustion have demonstrated some success in addressing this issue [2–7]. Optical engine images of the SACI combustion process show organized reaction fronts propagating away from the spark ignition source [2–4,7] during the initial front propagation phase of the process [4], with expansion speeds ranging from approximately 0.5 to 10 m/s [3,7]. This front propagation phase eventually transitions to a combustion process dominated by end-gas auto-ignition. The deflagrative behavior of the initial front is supported through experimental heat release rate analysis, which has shown the transition from the low to moderate initial heat release rates characteristic of flames to the rapid combustion rates characteristic of auto-ignition [3,4,8]. In addition, premixed laminar flame simulations have shown that the high preheat, ultra-dilute mixtures characteristic of those used in HCCI and SACI engines are capable of supporting laminar reaction fronts [8–10]. The magnitudes of the experimental SACI front expansion speeds are similar to those at both the main flame front and at the reaction fronts originating from end-gas ignition kernels in a spark-ignited engine undergoing mild to moderate knock [11] and are on the same order as the apparent expansion speeds of fronts originating from ignition kernels during the later portion of HCCI combustion [12].

The wide range of front speeds observed within the above studies suggests the potential for a variety of subsonic premixed combustion regimes within SI, SACI, and HCCI combustion, including the normal deflagration and spontaneous ignition front regimes [13]. The former regime is typical premixed flame propagation, governed by the diffusive–reactive balance within the reaction zone of the front, while the latter regime is a chemically controlled cascade of ignition events, also within a temperature gradient but with apparent propagation rates in excess of the laminar burning velocity.

A variety of computational studies have examined reaction front propagation into auto-igniting end-gasses. Early work by Pitz and Westbrook [14] examined the transient behavior of a laminar flame propagating into an auto-igniting end-gas. Significant reaction front acceleration was observed during the end-gas ignition; however, the study concentrated on the wall region and did not directly apply to the bulk gas combustion in HCCI engines. Various

* Corresponding author. Address: W.E. Lay Automotive Laboratory, 1231 Beal Avenue, Ann Arbor, MI 48109-2121, United States. Fax: +1 734 764 4256.
E-mail address: jmartz@umich.edu (J.B. Martz).

0010-2180/$ - see front matter © 2012 The Combustion Institute. Published by Elsevier Inc. All rights reserved.
doi:10.1016/j.combustflame.2012.01.011

computational studies have proposed methods of classifying the regime of the ignition front propagation during end-gas ignition, based on the temperature gradient [15], the front speed relative to the laminar flame speed [16,17], a characteristic Damköhler number [18], or the important index generated by the computational singular perturbation [19]. Unfortunately, these criteria rely upon detailed spatial and temporal information about the front which is not currently available within engine level simulations.

Recently, the authors used steady flow reactor simulations (PREMIX) to characterize the reaction front's combustion regime based on the upstream conditions at the front base [20]. These simulations showed that the burning velocity and front thickness increased with upstream reaction progress and temperature. A similar study was mentioned in a CFD-based modeling work of SACI combustion [21], where a one dimensional flame code was used to build a flamelet library of reaction fronts of various compositions and with unburned gas temperatures up to 1100 K. The one-dimensional flame results were combined with a G-equation model of turbulent combustion and used to simulate SACI engine experiments. Although the results were favorable, the apparent use of steady state laminar flame simulations as the basis of the flame model raises questions about the application to auto ignition situations, especially at times close to the auto ignition event.

While charge dilution with exhaust products has been favored by many pragmatic applications of SACI, a variety of fundamental SACI studies have chosen to use preheated air as the diluent [7,22–24]. Following these studies, air has been selected as the diluent in the present work. In addition, while gasoline is currently the primary fuel of passenger vehicles, its kinetic, thermophysical and transport properties remain variable and ill defined [25]. In this work, isooctane is used as a gasoline surrogate, given the comparable laminar burning velocities [26] and ignition delays [27] of the two fuels.

In the current study, a fully transient simulation is applied to a premixed, one-dimensional laminar reaction front propagating into an auto-igniting end-gas of an isooctane air mixture under the thermodynamic conditions of SACI combustion with both constant and variable domain pressures. This scenario is representative of a single reaction front within the turbulent flame brush [28] propagating into an auto-igniting upstream mixture as observed during SACI combustion [2–4,7,23]. While this one-dimensional simulation does not directly take turbulence into account, with the proper choice of timescales and pressure rise rates, it is useful as a model problem for understanding the thermodynamic behavior of turbulent flames, the underlying structure of which has been shown to be composed of wrinkled laminar flames in direct simulation [29,30]. Detailed analysis of the transient evolution of the front's burning velocity, maximum temperature gradient, thickness and structure can provide useful insight into the physical mechanisms present during the SACI combustion process. Additional studies on the sensitivity of the front's burning velocity to transport and a dynamic timescale analysis can be used to examine the combustion regime transition within the reaction front during end-gas auto-ignition.

2. Numerical method and simulation conditions

Reaction front simulations are performed with HCT [31], which solves the transient, one dimensional momentum, species and energy transport equations. An adaptive mesh refinement algorithm is employed to provide sufficient grid resolution within the reaction front; the computational mesh is composed of 75 cells, 30 of which are adaptive. Detailed chemistry is performed with the skeletal 215 species isooctane mechanism of Tham et al. [32], while TRANSPORT [33] is used to determine the mixture-averaged thermal conductivity and species diffusivities. Consistent with previous work [10], the mixture thermal conductivity is scaled by a factor of 0.8 in order to match the laminar burning velocities of experimental isooctane-air flames at atmospheric conditions [34,35]. In this previous work, the simulation was validated against high pressure ignition delay and stretch-corrected laminar burning velocity data.

The adopted model problem configuration is similar to that of Pitz and Westbrook [14], where the domain may be visualized as a one dimensional tube. At the initial simulation time t_0, the composition of the end-gas is fuel and air with zero reaction progress, while the thermal and compositional jump across the front are obtained from constant pressure equilibrium calculations. The reaction front propagates from the right to the left of the tube, where the left domain boundary, located at $x = 0$ cm, is adiabatic and impermeable, while the right boundary, located at x_{max}, is open and set to the domain pressure for the constant pressure cases. For the variable pressure case, the right boundary is configured to be adiabatic and impermeable, resulting in a closed-chamber simulation.

The time between spark discharge and the peak rate of heat release in SACI engine experiments [6,21] ranges from approximately 3 to 5 ms. The initial unburned conditions of the baseline case in

Table 1
The conditions examined within the current work and key simulation results.

Case	Φ	p (bar)	T_u (K)	T_{ad} (K)	t_{99} (ms)	SL_{steady} (cm/s)	HRR[b] ratio	Cond.[c] ratio	x_{max} (cm)	x_{disc} (cm)
1	0.45	20	1000	2007	3.8	66.2	0.98	0.14	0.320	0.289
2	0.80	20	373	2120	NA	14.4	NA	NA	0.101	0.071
3	0.30	20	1000	1703	5.4	26.7	1.01	0.09	0.277	0.208
4	0.35	20	1000	1808	4.7	37.5	1.00	0.10	0.280	0.231
5	0.40	20	1000	1909	4.2	50.9	1.00	0.15	0.297	0.260
6	0.45	30	1000	2007	2.7	55.1	1.02	0.14	0.200	0.177
7	0.45	40	1000	2007	2.1	48.5	1.01	0.09	0.144	0.125
8	0.45	50	1000	2008	1.8	44.0	1.01	0.08	0.112	0.096
9	0.45	20	900	1917	21.1	39.9	1.00	0.11	0.938	0.901
10	0.45	20	925	1940	13.4	45.4	1.02	0.14	0.695	0.660
11	0.45	20	950	1962	8.7	51.6	1.00	0.15	0.525	0.491
12	0.45	20	975	1984	5.7	58.5	0.99	0.14	0.405	0.373
13	0.45	20	1025	2030	2.6	74.7	0.97	0.14	0.257	0.228
14	0.45	20	1050	2052	1.8	84.2	0.97	0.13	0.210	0.182
15	0.45	20[1]	1000[a]	NA	NA	NA	0.98	0.22	0.230	0.199

[a] Initial conditions for the variable pressure case.
[b] HRR Ratio: The ratio of the peak heat release rate within the front relative to that of the end-gas, at t_{qmax}.
[c] Cond. Ratio: The ratio of the peak heat conduction rate within the front, at t_{qmax} relative to that at steady front propagation. For Case 15, this ratio is defined as the peak heat conduction rate within the front at t_{qmax} relative to the maximum observed value.

this work, Case 1 in Table 1, are selected to approximate these timescales, where the time from t_0 to t_{99}, the time of 99 % end-gas reaction progress (c_{eg}), is 3.8 ms. The Case 1 unburned conditions correspond to a constant pressure, p, of 20 bar, an initial end-gas temperature, T_u, of 1000 K, and an equivalence ratio, Φ, of 0.45, in line with the optical engine experiments of Zigler et al. [7]. Additional parametric conditions under study are also summarized in Table 1. Case 2 is performed to provide a comparison with a conventional flame, simulated under the conditions reported in Jerzembeck et al. [26]. Additional runs are performed, where Φ, p, T_u and T_{ad}, the adiabatic flame temperature, are selected to be relevant to SACI combustion. Cases 3–5 sweep through a range of Φ for the same p and T_u, Cases 6 through 8 are considered to investigate the effect of pressure, while Cases 9 through 14 explore the effect of T_u, where the lowest T_u is selected to produce combustion timescales comparable to those observed in the ultra-lean rapid compression facility study of reaction front propagation into an auto-igniting end-gas [24]. Finally, Case 15 is performed to examine the effect of time varying pressure and temperature on the front propagation process.

For the constant pressure, auto-igniting cases, x_{max} is selected through the use of the burning velocity and thickness correlations from [10], along with constant pressure ignition delay simulations. The minimum upstream and downstream front/boundary offset is selected through a grid sensitivity analysis performed on the base case, where the minimum front/boundary offset ranges from 5 to 30 reaction front thicknesses. Burning velocities were found to be largely grid-independent, with the largest variations occurring around the time of the peak burning velocity. Relative to that of the finest mesh, the differences in the peak burning velocity range from −2% to +1%. Ultimately, the mesh with a minimum upstream and downstream offset of 7.5 front widths is selected for the constant pressure cases to provide the best compromise between numerical accuracy and maximum front/boundary offset.

To ensure that the front remains within the domain during the initial stages of the simulation, the initial thermal and compositional discontinuity is situated at x_{disc}, 7.5 front thicknesses upstream of the domain's right boundary. To prevent front/boundary interaction [36], x_{max} is sized to accommodate the predicted front travel plus an additional 7.5 front thicknesses for the constant pressure cases. In addition, x_{max} is sufficiently long so that the front is not displaced out of the domain's right hand boundary by end-gas expansion during auto-ignition. The front location and the domain's thermal profile are visualized for each run to ensure the absence of flame boundary interaction.

Using the gas and burning velocity at the reaction front position, u_f, and S_b, respectively, the time rate of change of the reaction front position in the laboratory frame, S_f, can be calculated with $S_f = S_b - u_f$. For the constant pressure cases, the front position is specified as the location of the average temperature between the end-gas and maximum temperature of the domain, T_b. Relative to the end-gas, the laminar burning velocity, S_L, is obtained for quasi-steady front propagation using the density at the reaction front position and the density of the end-gas, ρ_f and ρ_u, where $S_L = \rho_f S_f / \rho_u$. End-gas properties are obtained from the left most cell of the domain.

The thermal front thickness, δ, is defined for the constant pressure cases as the distance between the beginning and end of the reaction front, where the front beginning is defined as the location where the domain temperature is equivalent to T_{eg}, the instantaneous end-gas temperature, plus 1% of T_u, while the front end is defined by the location where the domain temperature is 99% of T_b. The end-gas reaction progress, c_{eg}, is defined with the following equation:

$$c_{eg} = \frac{T_{eg} - T_u}{T_{ad} - T_u} \tag{1}$$

3. Constant pressure simulation results

The time-dependent evolution of the domain's temperature profile for Case 1 is shown in Fig. 1a. The reaction front travels from the right to the left of the domain, where the increase in end-gas temperature (T_{eg}) results from end-gas heat release. The burning velocity of the front remains almost constant during this time, indicated by the front's nearly uniform temporal movement. Beyond T_{eg} = 1100 K, corresponding to a simulation time of 3.544 ms, the end-gas is rapidly consumed by auto-ignition, and combustion is nearly completed by a t_{99} of 3.819 ms. Figure 1b shows a magnified view of the temperature profile around the front at five select times during end-gas auto-ignition, beginning at 3.544 ms. As auto-ignition proceeds, a reduction of the temperature gradient within the front is apparent, while beginning around 3.784 ms, the front is displaced to the right of the domain as the rate of end-gas expansion at the front exceeds the front's burning velocity. Domain gas velocities remain low throughout the auto-ignition process, where the peak observed Mach number is less than 0.01. The slight temperature dip observed upstream of the reaction front beginning around a T_{eg} of 1500 K is attributed to numerical errors within the solution.

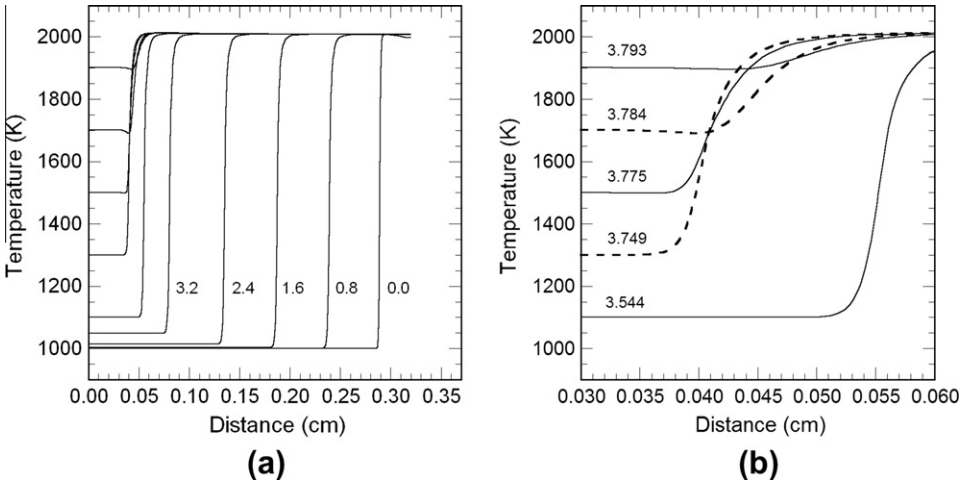

Fig. 1. (a) Evolution of the temperature profile for Case 1 at T_u = 1000 K, p = 20 bar, Φ = 0.45. (b) Magnified view of the local temperature profile around the front during auto-ignition. Times are indicated on the figure in milliseconds.

Around 0.7 ms into the simulation, the Case 1 reaction front attains a steady burning velocity of 66.1 cm/s, where the steady front thickness and maximum temperature gradient are 1.15×10^{-2} cm and 3.03×10^{5} K/cm, respectively. Once the front attains a steady S_L, these quantities show little change through 3.5 ms of the simulation. Fig. 2a shows the temporal evolution of T_{eg}, the maximum temperature gradient within the reaction front, dT/dx_{max}, and the thermal front thickness, δ, from 3.5 to 4.0 ms, while Fig. 2b shows the end-gas reaction progress, c_{eg}, the rate of end-gas heat release, $ROHR_{eg}$, and the reaction front burning velocity, S_L. Relative to steady front propagation, a significant decrease in dT/dx_{max} and an increase in S_L are observed at the time of the end-gas maximum rate of heat release (e.g. chemical power), t_{qmax}, when $T_{eg} = 1641.4$ K and $c_{eg} = 63.7$ %. It is seen that δ remains constant prior to t_{qmax}, after which it decreases rapidly. The burning velocity peaks at 512.5 cm/s, increasing by 7.8 times from the steady S_L, while dT/dx_{max} has decreased by a factor of 19.2. The drastic changes in dT/dx_{max} and S_L suggest a transition to the spontaneous ignition front regime [13], where the spatial gradients in temperature and composition are low, consistent with minimal transport effects [15]. Considering the insignificant change in δ up to this point in time, the decrease in dT/dx_{max} is attributed primarily to the reduction in the difference between T_{eg} and T_b. While moderate burning velocities are observed late into the end-gas combustion process, front propagation is complete by 4 ms, when $c_{eg} = 100\%$. The evolution of T_{eg}, dT/dx_{max} and S_L of the additional constant pressure cases all show similar trend-wise behavior to that of Case 1.

The steady burning velocities observed for the constant pressure runs prior to t_{qmax} suggest that the initial fronts are within the normal deflagration regime; the S_L values for these steady fronts are shown in Table 1. Fig. 3 shows the local rates of sensible energy change associated with reaction and heat conduction compared between two flames with similar T_{ad}. Case 1 represents a SACI flame while Case 2 represents a normal SI flame, with rates non-dimensionalized by the maximum heat release rate of the steady front in Case 2 at 3.15×10^{12} erg/cm^3 -s. Defining the reaction zone thickness to be the distance between the upstream and

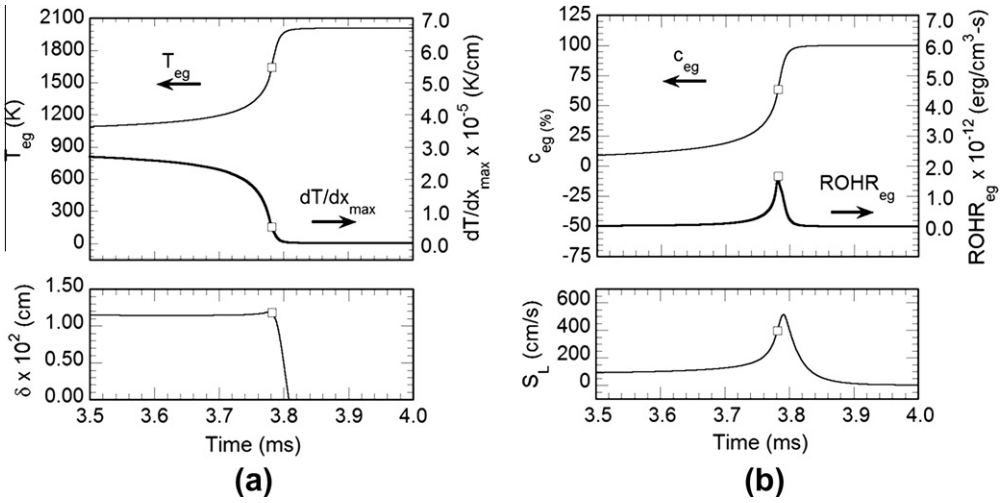

Fig. 2. The transient evolution of the reaction front and end-gas for Case 1 at $T_u = 1000$ K, $p = 20$ bar, $\Phi = 0.45$, where t_{qmax} is marked on the figure with a square at 3.782 ms: (a) T_{eg}, dT/dx_{max} and δ as a function of time and (b) c_{eg}, $ROHR_{eg}$ and S_L as a function of time.

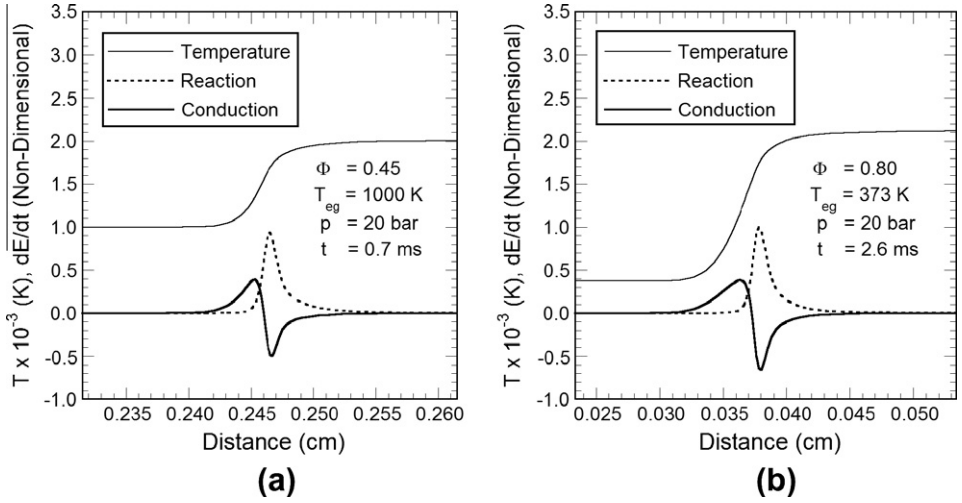

Fig. 3. Comparison of the temperature profiles and non-dimensionalized rates of sensible energy change associated with reaction and heat conduction in proximity to two steady reaction fronts with similar adiabatic flame temperatures: (a) the front under SACI conditions (Case 1) at $T_u = 1000$ K, $p = 20$ bar, $\Phi = 0.45$ and (b) the front under SI conditions (Case 2) at $T_u = 373$ K, $p = 20$ bar, $\Phi = 0.80$.

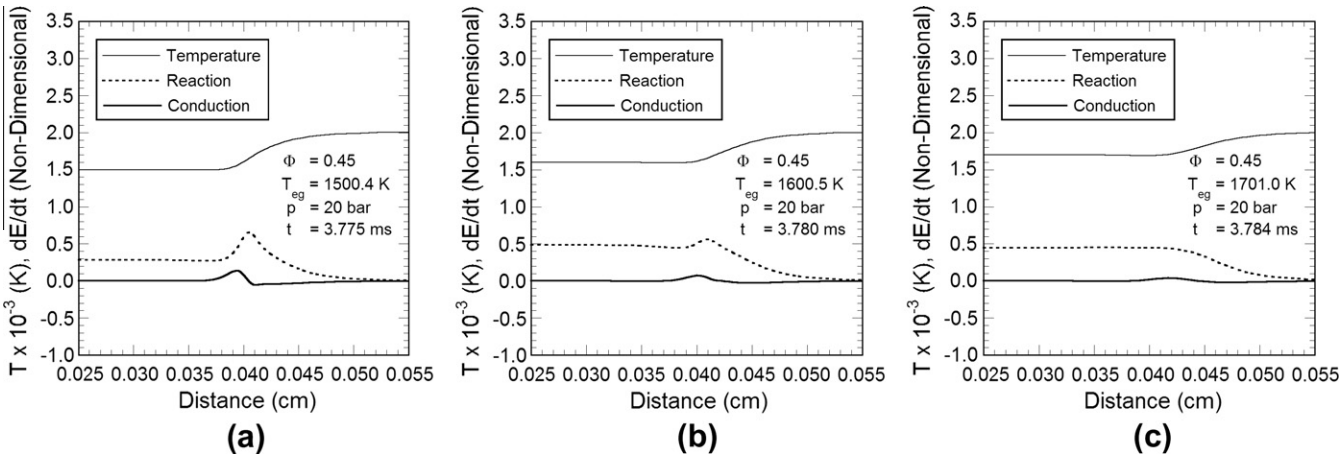

Fig. 4. Evolution of the temperature profile and non-dimensionalized rate of sensible energy change due to reaction and heat conduction in proximity to the reaction front during end-gas auto-ignition for Case 1 at T_u = 1000 K, p = 20 bar, Φ = 0.45 for T_{eg} of: (a) 1500.4 K (3.775 ms), (b) 1600.5 K (3.780 ms) and (c) 1701.0 K (3.784 ms), where t_{qmax} occurs at 3.782 ms (1641.4 K).

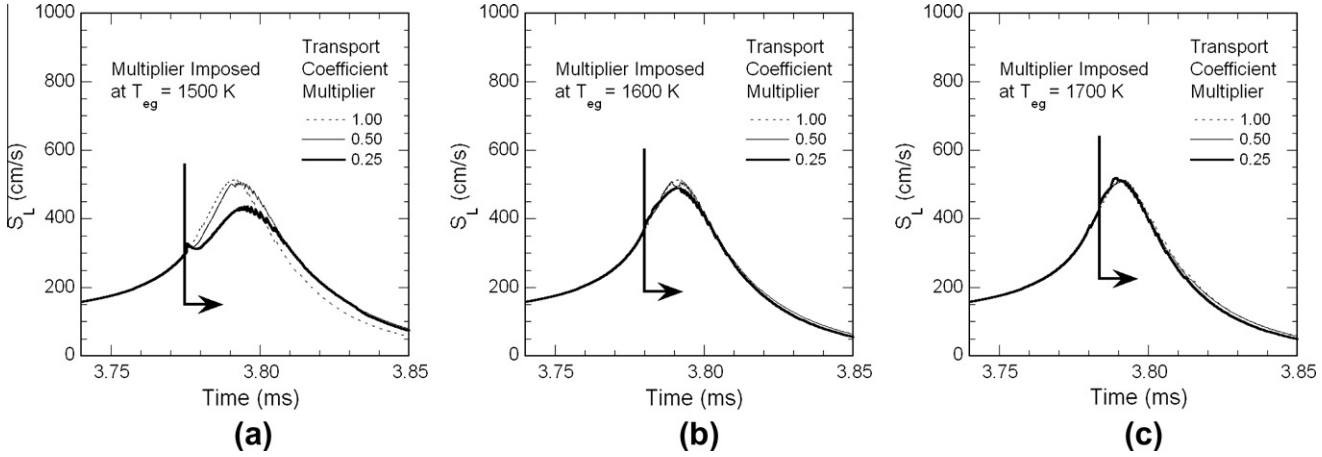

Fig. 5. The effect of transport on the burning velocity of Case 1 at T_u = 1000 K, p = 20 bar, Φ = 0.45, where the vertical line marks the time when the transport coefficients are modified, in this case at a T_{eg} of: (a) 1500 K, (b) 1600 K and (c) 1700 K. The burning velocity's lack of sensitivity to the transport coefficient magnitudes beyond t_{qmax} of 3.782 ms (1641.4 K) indicates apparent front propagation within the spontaneous ignition front regime.

downstream locations where the rate of heat release is 1% of the peak value, similar reaction zone thicknesses are observed between Cases 1 and 2, 1.06×10^{-2} cm and 1.00×10^{-2} cm, respectively. The shorter preheat zone for the Case 1 SACI front, 0.87×10^{-3} cm vs. 1.02×10^{-2} cm for Case 2 results from the fact that less preheating of the upstream mixture is required for the high T_u of the SACI front. Despite these small differences, the deflagrative nature of both fronts is clearly evident.

To understand the physical mechanisms governing reaction front propagation during end-gas auto-ignition, Fig. 4 shows the spatial profiles of temperature and the rates of sensible energy change associated with reaction and heat conduction for Case 1 at three different times near t_{qmax}. Energy rates are non-dimensionalized as those in Fig. 3. Starting from a deflagrative structure at 3.775 ms, shown in Fig. 4a, an increase in the end-gas heat release rate is evident in subsequent times, and at 3.784 ms the heat release profile becomes monotonic, indicating that end-gas auto-ignition is the dominant mechanism for heat release. The 3.780 ms and 3.784 ms cases bound the time of the end-gas maximum chemical power, t_{qmax}, which occurs at 3.782 ms. The ratio of the peak rate of heat release in the front to $ROHR_{eg}$ at t_{qmax} is 0.98 for Case 1; this ratio is similar for the other cases, as shown in Table 1. The reduction in the conductive heat transfer rate is mainly due to the decrease in dT/dx_{max} observed in Fig. 2. As shown in Table 1 for Case 1, the peak heat conduction rate within the front at t_{qmax} is 14% of that observed at the steady state deflagration condition, indicating that a transition from the flame front to end-gas auto-ignition has occurred. As shown in Table 1, the other cases display similar behavior. Because of the remaining temperature gradients within the front, heat conduction remains finite throughout the combustion process. Nevertheless, the absence of the heat release peak at the ignition front beyond t_{qmax}, as shown in Fig. 4c, clearly demonstrates that ignition beyond this time is chemically-controlled, such that t_{qmax} would seem a reasonable criterion to identify the transition from deflagration to spontaneous ignition regimes. All of the other constant-pressure SACI relevant cases show consistent behavior.

To confirm that t_{qmax} is indeed a good marker to identify the combustion regime transition, additional tests have been conducted to assess the sensitivity of combustion within the front to transport. At a specific time during the unsteady calculation, the transport coefficients are artificially reduced by a constant multiplication factor of 0.5 and 0.25 for the remaining calculations. Fig. 5 shows the results of this exercise for Case 1, where the transport coefficient multipliers are applied at the times when T_{eg} reaches (a) 1500 K, (b) 1600 K, and (c) 1700 K, respectively. The

vertical lines indicate the time at which the multipliers are applied. Fig. 5a shows that S_L is significantly affected by the modified transport, while Fig. 5b and c shows minimal changes. These results are consistent with those in Fig. 4, demonstrating that for times prior to t_{qmax}, when $T_{eg} \approx 1641$ K, heat conduction impacts energy transfer within the front and that S_L is sensitive to transport – a characteristic of combustion within the normal deflagration regime. Beyond t_{qmax}, however, S_L is relatively insensitive to transport while heat conduction within the front is shown to be nearly negligible, implying that the front at this condition is within the chemically controlled, spontaneous ignition front regime.

4. Variable pressure simulation results

In real engines, the system pressure rises as the combustion process proceeds. To assess the validity of the findings in Section 3 for real engine conditions, Case 15 was examined as a variable pressure, closed system simulation. The choice of initial conditions and the domain length result in an overall simulation time for Case 15 of approximately 1.2 ms corresponding to 14 crank angle degrees for an engine running at 2000 rpm. The average pressure rise rate is approximately 20 bar/ms or 1.7 bar/deg, comparable to typical engine conditions. While the closed-chamber 1D simulation cannot reproduce the variable volume constraint occurring in real engines, it is considered here as a limiting case study with the maximum effects of heat release-induced compression. The real engine combustion condition would fall between the constant and variable pressure simulations presented here.

Figure 6 shows the temporal evolution of various quantities for Case 15, to be compared with the constant pressure results for Case 1 shown in Fig. 2. Because of the temperature gradient that develops behind the flame within the burned gases due to compression heating (not shown), δ is defined as the distance between the upstream and downstream locations of the absolute value of 2% of the peak heat conduction rate (see Fig. 3). When applied to Case 1, this thickness definition produces results similar to the thermal δ metric described in Section 2. Compared with Fig. 2, the burning-induced pressure rise results in a more rapid increase in T_{eg} and ROHR_{eg}. Furthermore, a steady decrease in δ during the deflagration phase (up to 1.14 ms) is seen. Despite these quantitative differences, the main characteristics of dT/dx_{max}, ROHR_{eg} and S_L near and beyond t_{qmax} remain consistent with those in Fig. 2.

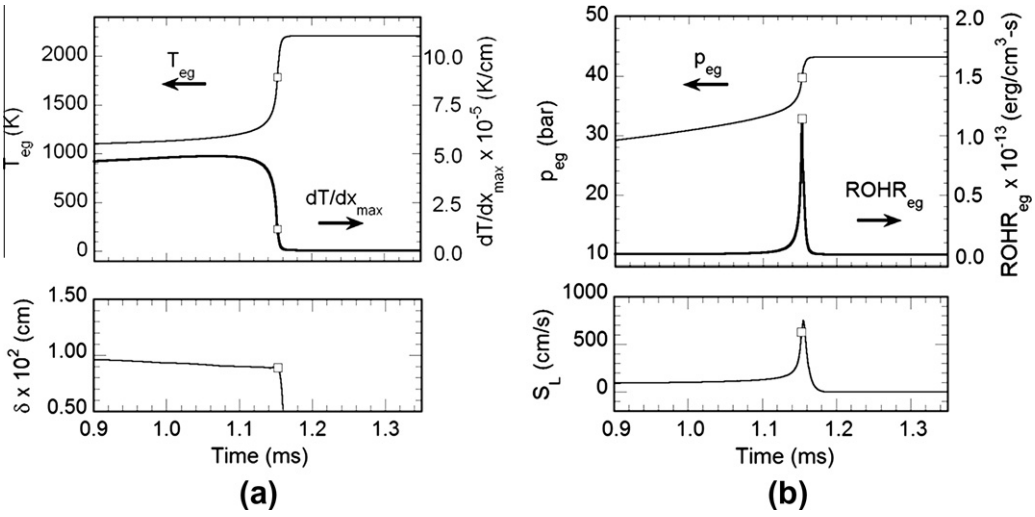

Fig. 6. The transient evolution of the reaction front and end-gas for the variable pressure system, Case 15 at $T_u = 1000$ K, the initial end-gas pressure $p_u = 20$ bar, $\Phi = 0.45$, where t_{qmax} is marked with a square on the figure at 1.153 ms. (a) T_{eg}, dT/dx_{max} and δ as a function of time. (b) The end-gas pressure, p_{eg}, $ROHR_{eg}$ and S_L as a function of time.

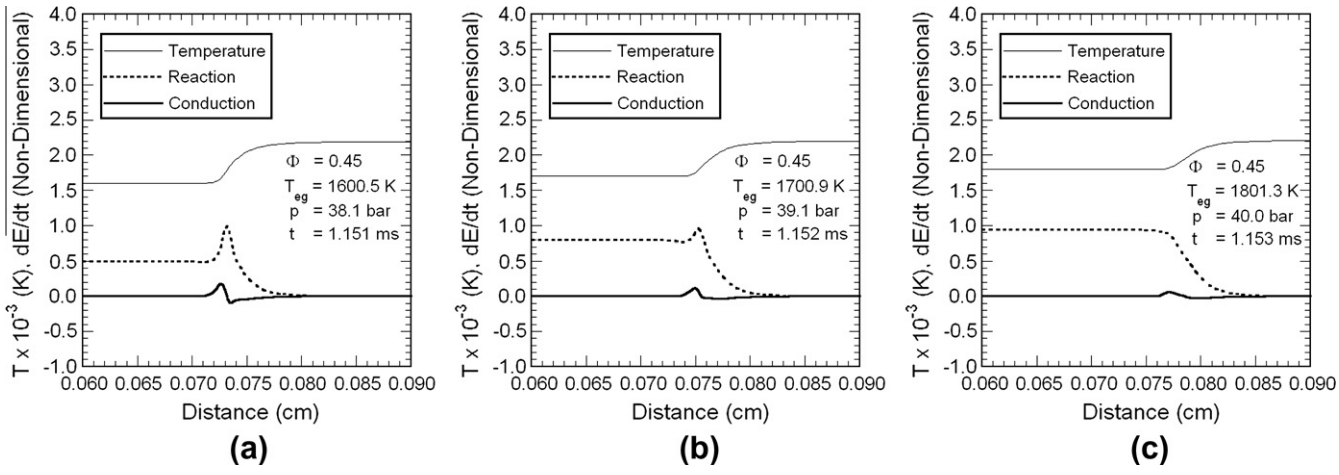

Fig. 7. Evolution of the temperature profile and non-dimensionalized rate of sensible energy change due to reaction and heat conduction in proximity to the reaction front for the variable pressure system, Case 15 at $T_u = 1000$ K, $p_u = 20$ bar, $\Phi = 0.45$ for T_{eg} of: (a) 1600.5 K (1.151 ms), (b) 1700.9 K (1.152 ms) and (c) 1801.3 K (1.153 ms), where t_{qmax} is observed at 1.153 ms ($T_{eg} = 1781.6$ K).

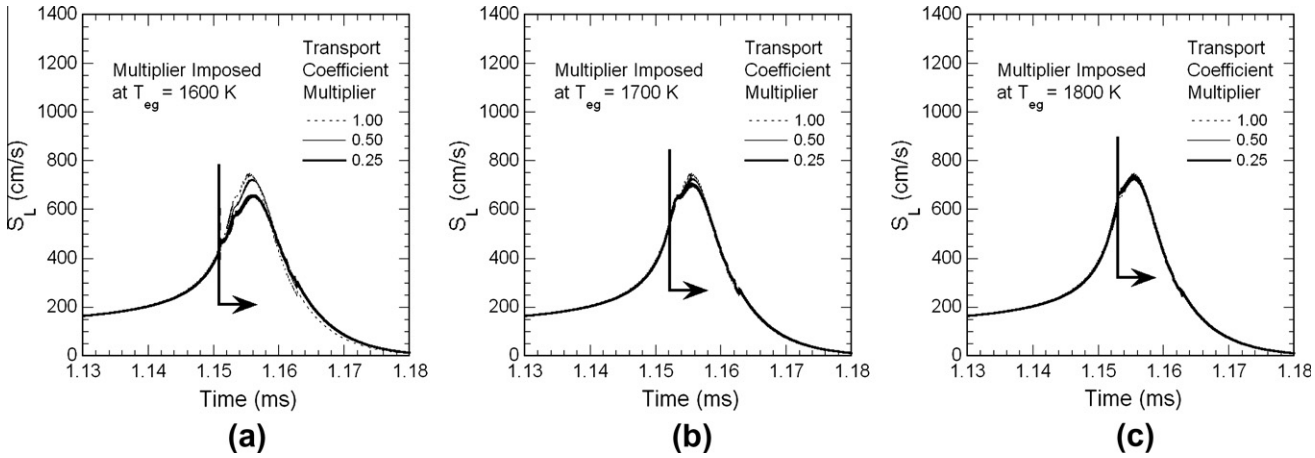

Fig. 8. The effect of transport on burning velocity for the variable pressure system, Case 15 at T_u = 1000 K, p_u = 20 bar, Φ = 0.45, where the vertical line marks the time when the transport coefficients are modified, in this case at end-gas temperatures of: (a) 1600 K, (b) 1700 K and (c) 1800 K. The burning velocity's lack of sensitivity to the transport coefficient magnitudes beyond t_{qmax} of 1.153 ms (T_{eg} = 1781.6 K) indicates apparent front propagation within the spontaneous ignition front regime.

Figure 7 shows the equivalent of Fig. 4 for Case 15. Again, the evolution of end-gas reaction near t_{qmax} is consistent with those in Fig. 4, such that a transition from deflagration to spontaneous ignition at t_{qmax} is evident. Fig. 8 further shows the sensitivity of S_L to the modified transport coefficients for Case 15, to be compared with Fig. 5. A consistent result is found in that the sensitivity to transport coefficients becomes minimal as the modification is applied at T_{eg} = 1700 K and above, that is at $t = t_{qmax}$ and beyond, thus confirming that t_{qmax} adequately identifies the transition time of the combustion regimes for the variable pressure case. Note that the maximum observed pressure rise rate of 111.9 MPa/ms at 1.153 ms in Fig. 6b significantly exceeds the limiting pressure rise rates within practical low temperature combustion engines, which are on the order of 5 MPa/ms [37]. Nevertheless, the reaction front behavior remains similar to the constant pressure combustion results. Considering that the present variable pressure case study captures a more extreme scenario than that observed in a real SACI engine, it is expected that the findings in the constant pressure simulation studies are valid under real engine conditions.

5. Timescale analysis

A suitable timescale for characterizing a deflagration can be defined with τ_{front}, the time for the front to travel its thickness as defined by the following equation:

$$\delta = \int_{t_0}^{t_0+\tau_{front}} S_L(t)dt \tag{2}$$

For a steady flame during the above time interval, S_L is constant and the characteristic front time reduces to $\tau_{front} = \delta/S_L$. Fig. 9a shows the rapid evolution in T_{eg}, dT/dx_{max} and S_L during auto-ignition for Case 1 occurring within approximately one characteristic front time, defined in this case with steady flame properties. Fig. 9b shows similar behavior for the variable pressure case, where τ_{front} is defined with the time weighted average of the flame properties during the deflagrative front propagation period, when the end-gas rate of heat release is less than 0.1% of the maximum (see Fig. 6). Fig. 10a shows the timescales of the total combustion duration ($t_{99} - t_0$) normalized by τ_{front} for the SACI cases. Because of the temperature gradient within Case 15, t_{99} is selected late in the end-gas reaction progress, at the time when $ROHR_{eg}$ is at 2% of its maximum value. Both methods for t_{99} agree well when applied to Case 1. For all auto-igniting cases under study, the total combustion duration is much longer than τ_{front}. Fig. 10b also shows the normalized timescale $(t_{99} - t_{qmax})/\tau_{front}$, equal to the lifetime of the spontaneous ignition front. This timescale is much smaller, ranging from 0.09 to 0.27 front times, thus indicating that the duration of ignition front propagation is small relative to τ_{front}.

A timescale analysis has been conducted as an alternative metric to identify the combustion regime transition. In addition to τ_{front} defined above, a chemical timescale, τ_{chem}, is defined to measure the remaining chemical lifetime of the end-gas, and is determined as the time from the instantaneous solution time t to t_{99} (the time for 99% reactant depletion in the end-gas). In the normal deflagration regime, $\tau_{front} \ll \tau_{chem}$ as the reactive–diffusive nature of the front results in the faster chemical processing of an adjacent unburned mixture relative to the time for this mixture to be consumed by auto-ignition. In contrast, within the spontaneous ignition front regime, once ignition dominates combustion within the front, the remaining time required for the spontaneous ignition wave to traverse a given δ should be the same as the time required for the end-gas to be consumed by auto-ignition, hence $\tau_{front} \approx \tau_{chem}$.

Figure 11a shows T_{eg}, τ_{chem} and τ_{front} as a function of time from 1 to 4 ms for Case 1, where τ_{front} is calculated with the instantaneous δ and S_L. For the first 3.5 ms of the simulation, τ_{chem} exceeds τ_{front}, implying that the front is in the deflagration regime. At approximately 3.7 ms, which is close to t_{qmax}, the two timescales become comparable, indicating that combustion within the front has transitioned to the chemically controlled regime.

Unlike previous steady flow reactor simulations [20], the deflagrative front thickness of the transient solutions varies little during end-gas auto-ignition. The thickening observed for the steady front solutions during auto-ignition is attributable to the infinite time available for the adjustment to a steady solution. Perhaps even more importantly, the mixture residence times and end-gas reaction progress during auto-ignition are axially dependent within the steady flow reactor system, while residence times within the transient domain are uniform, leading to different end-gas temperature profiles during auto-ignition. Considering the compression of the adiabatic mixture core within an internal combustion engine, the uniform residence time of the transient solution provides a more engine-relevant temperature profile upstream of the front. Flame time calculations using simple metrics such as δ/S_L obtained from the steady flow reactor during auto-ignition may lead to excessively large front times, resulting in a timescale inversion rather than convergence at the transition to chemically controlled combustion within the front.

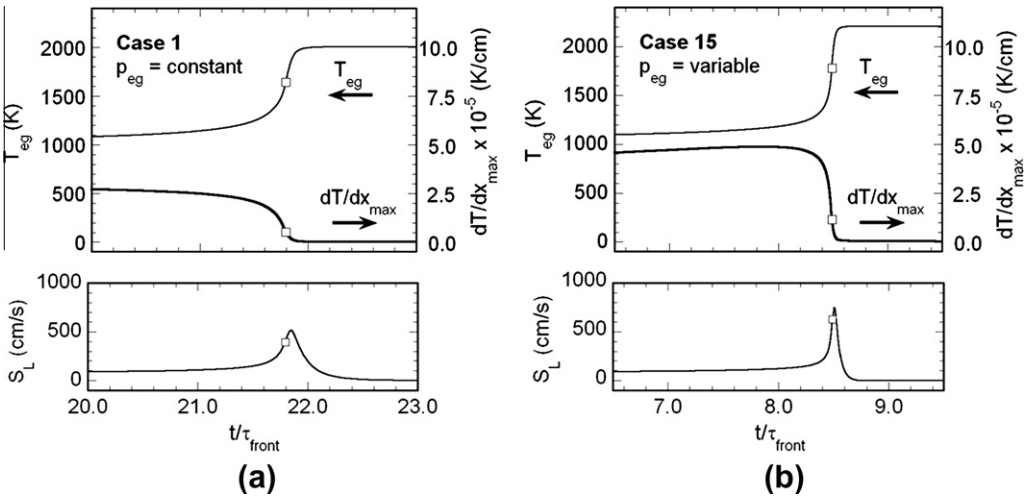

Fig. 9. The transient evolution of T_{eg}, dT/dx_{max} and S_L as a function of time in front times for: (a) Case 1 at constant pressure and (b) Case 15 at variable pressure. For both cases, T_u = 1000 K, p_u = 20 bar, Φ = 0.45, where t_{qmax} is marked with a square on the figure.

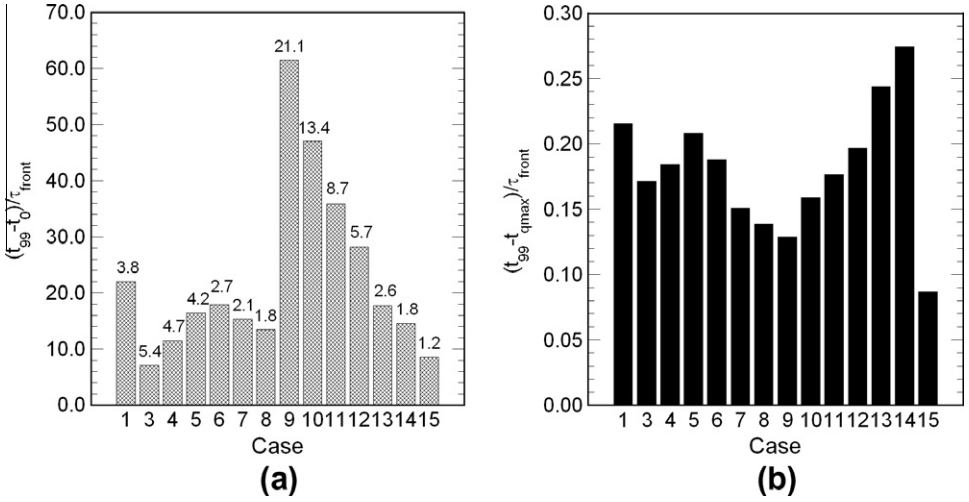

Fig. 10. (a) Time intervals in front times for reaction front propagation through t_{99} for Cases 1, 3–15, where t_{99} is shown on the figure in milliseconds above each case. (b) The time interval for ignition front propagation in front times for Cases 1, 3–15.

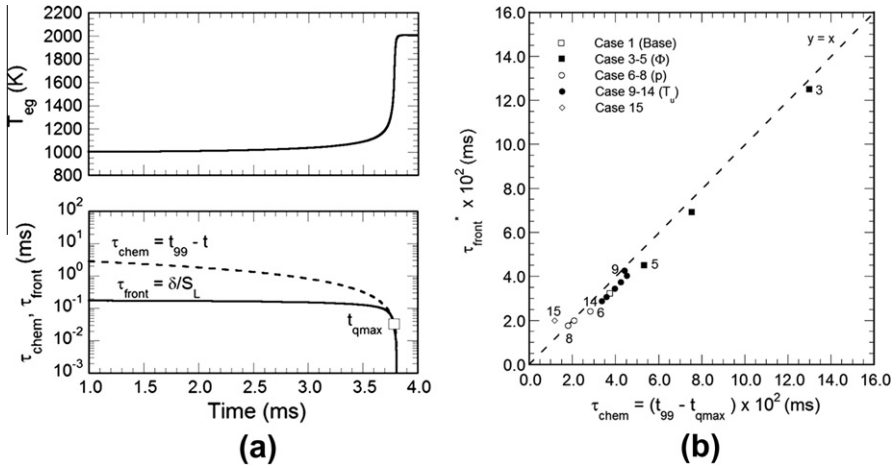

Fig. 11. (a) T_{eg}, τ_{front} and τ_{chem} shown from 1.0 to 4.0 ms for Case 1, with t_{qmax} shown at 3.782 ms. (b) The dynamic reaction front timescale, τ^*_{front} vs. τ_{chem} defined at t_{qmax}, with select case numbers adjacent to data points. The timescales decrease with increasing Φ, p or T_u.

Considering that significant variations occur in S_L during auto-ignition, a more relevant front timescale, τ^*_{front}, is defined with the following equation:

$$\delta_{tqmax} = \int_{t_1}^{t_1+\tau^*_{front}} S_L(t)dt \quad (3)$$

where t_1 is selected so that $t_1 + \tau^*_{front} = t_{99}$. In other words, τ^*_{front} is the time required for the front to travel a distance equal to δ at t_{qmax}, just prior to t_{99}. Similar to the above, t_{99} is selected for Case 15 late in the end-gas combustion process, when the $ROHR_{eg}$ has decreased to 2% of its maximum value. The use of t_{99} and 2% of the maximum $ROHR_{eg}$ yield similar τ^*_{front} when applied to Case 1. If t_1 is equal to t_{qmax}, then τ^*_{front} and τ_{chem} are also equivalent, indicating that the time for the mixture within the front and the end-gas to be converted to products is the same. The similarity between τ^*_{front} and τ_{chem} in Fig. 11b confirms the agreement between t_1 and t_{qmax}, verifying the suitability of t_{qmax} as a combustion regime transition parameter.

The above results demonstrate that early in the combustion process, $\tau_{front} \ll \tau_{chem}$. During this time, the front is within the normal deflagration regime; consuming end-gas mass and propagating several front thicknesses as shown in Fig. 10a. Around t_{qmax}, when $\tau_{front} \approx \tau_{chem}$ for the cases shown in Fig. 11b, the sequential auto-ignition process of the spontaneous ignition front is confined to one front thickness as diffusion has been marginalized.

Within a SACI engine, a large fraction of the overall energy release results from auto-ignition [5]. Considering the elevated end-gas reaction progress during spontaneous ignition front propagation, and the small fraction of mass within the reaction front relative to the overall system mass, even if a transition to a spontaneous ignition front from the initial deflagration wave is commonly encountered, such a spontaneous front will likely contribute to only a small fraction of the overall energy release. In the context of sub-grid level CFD modeling of the spontaneous ignition front, these results indicate that a bi-modal switch from flame propagation to homogeneous reactor models can be employed without a significant loss of fidelity at the transition to chemically controlled combustion within the front, given the similar chemical and front timescales observed at t_{qmax}.

6. Conclusions

To better understand the process of premixed reaction front propagation during end-gas auto-ignition, transient one dimensional reaction front simulations were performed under thermodynamic conditions relevant to SACI combustion for both constant and variable system pressures. For all simulation cases, the reaction front began as a deflagration. The thicknesses of the deflagrative constant pressure fronts varied little during end-gas auto-ignition, while the maximum temperature gradient within the fronts diminished with end-gas reaction progress and the accompanying rise in T_{eg}. As a result of the diminishing temperature gradient, heat conduction within the front subsided with reaction progress and combustion within the front eventually became chemically controlled. A novel metric was defined to quantify the front's transition from deflagrative to chemically controlled combustion at the time of the end-gas maximum chemical power through the inspection of peak heat conduction magnitudes and the sensitivity of the front's burning velocity to transport. While significant increases in burning velocity were observed with end-gas reaction progress, τ_{front} and τ_{chem} were found to be nearly equivalent at the onset of chemically controlled combustion within the front. Therefore, at the transition to the spontaneous ignition front regime, the ignition wave travels only one front thickness within the remaining chemical lifetime of the end-gas. Considering the high level of end-gas reaction progress during spontaneous ignition front propagation, the contribution of the spontaneous ignition front to the overall energy release is relatively insignificant since the mass contained within the reaction front is small. Results from the variable pressure simulation showed similar behavior, suggesting that the main findings from the constant pressure simulations are applicable to real SACI engines.

Acknowledgments

This work was sponsored by the Department of Energy under the University Consortium on Low Temperature Combustion for High Efficiency, Ultra-Low Emission Engines, directed by the University of Michigan under agreement *DE-FC26-06NT42629*. The authors gratefully acknowledge Professor J.Y. Chen of University of California, Berkeley for providing the skeletal isooctane mechanism, and Drs. William Pitz and Charles Westbrook of The Lawrence Livermore National Laboratory for the provision of HCT and discussions on the topic. The authors also wish to thank Dr. David Reuss of the University of Michigan for the many helpful discussions.

References

[1] F. Zhao, T.N. Asmus, D.N. Assanis, J.E. Dec, J.A. Eng, P.M. Najt, Homogeneous Charge Compression Ignition (HCCI) Engines: Key Research and Development Issues, PT-94, Society of Automotive Engineers International, Warrendale, PA, 2003.
[2] B.T. Zigler, S.M. Walton, X. He, J.T. Wiswall, M.S. Wooldridge, S.T. Wooldridge, Crank-Angle Resolved Imaging of Homogeneous Charge Compression Ignition Phenomena in a Single-Cylinder Research Engine, Tech. Meeting, CSS, The Combustion Institute, Cleveland OH, May 21–23, 2006.
[3] H. Persson, A. Hultqvist, B. Johansson, A. Remón, SAE 2007–01-0212, 2007.
[4] D.L. Reuss, T.W. Kuo, G. Silvas, V. Natarajan, V. Sick, J. Eng. Res. 9 (2008) 409–434.
[5] H. Yun, N. Wermuth, P.M. Najt, SAE 2010–01-0847, 2010.
[6] L. Manofsky, J. Vavra, D. Assanis, Babajimopoulos, A., SAE 2011–01-1179, 2011.
[7] B.T. Zigler, P.E. Keros, K.B. Helleberg, M. Fatouraie, D. Assanis, M.S. Wooldridge, J. Eng. Res. 12 (2011) 353–375.
[8] Y. Huang, C.J. Sung, J.A. Eng, Combust. Flame 136 (2004) 457–466.
[9] Y. Huang, C.J. Sung, K. Kumar, Combust. Sci. Technol. 179 (2007) 2361–2379.
[10] J.B. Martz, R.J. Middleton, G.A. Lavoie, A. Babajimopoulos, D.N. Assanis, Combust. Flame 158 (2011) 1089–1096.
[11] G. König, R.R. Maly, D. Bradley, A.K.C. Lau, C.G. W. Sheppard, SAE 902136, 1990.
[12] A. Hultqvist, M. Christensen, B. Johansson, M. Richter, J. Nygren, J. Hult, M. Aldén, SAE 2002–01-0424, 2002.
[13] Y.B. Zel'dovich, Combust. Flame 39 (1980) 211–214.
[14] W.J. Pitz, C.K. Westbrook, in: J.R. Bowen, J.C. Leyer, R.I. Soloukhin (Eds.), Dynamics of Reactive Systems Part II: Modeling and Heterogeneous Combustion, Progress in Astronautics and Aeronautics series, vol. 105, American Institute of Aeronautics and Astronautics, Inc., New York, 1986, p. 293–303.
[15] X.J. Gu, D.R. Emerson, D. Bradley, Combust. Flame 133 (2003) 63–74.
[16] R. Sankaran, H.G. Im, E.R. Hawkes, J.H. Chen, Proc. Combust. Inst. 30 (2005) 875–882.
[17] J.H. Chen, E.R. Hawkes, R. Sankaran, S.D. Mason, H.G. Im, Combust. Flame 145 (2006) 128–144.
[18] G. Bansal, H.G. Im, Combust. Flame 158 (2011) 2105–2112.
[19] S. Gupta, H.G. Im, M. Valorani, Proc. Combust. Inst. 33 (2011) 2991–2999.
[20] J.B. Martz, H. Kwak, H.G. Im, G.A. Lavoie, D.N. Assanis, Proc. Combust. Inst. 33 (2011) 3001–3006.
[21] R. Dahms, C. Felsch, O. Röhl, N. Peters, Proc. Combust. Inst. 33 (2011) 3023–3030.
[22] M. Weinrotter, E. Winter, K. Iskra, T. Neger, J. Olofsson, H. Seyfried, M. Aldén, M. Lackner, F. Winter, A. Vressner, A. Hultqvist, B. Johansson, SAE 2005–01-0129, 2005.
[23] P. Keros, D. Assanis, J. Schlechtweg, M.S. Wooldridge, Fast Methods to Analyze High-Speed Images of HCCI and Spark-Assisted HCCI Ignition Events, 2010 Fall Technical Conference, ICED, ASME, San Antonio, TX September 12–15, 2010.
[24] D. Assanis, S. Wagnon, M.S. Wooldridge, Investigation of Flame Propagation under High Pressure Conditions in a Rapid Compression Facility using High-Speed Optical and Pressure Diagnostics, Proceedings of the 7th US National Combustion Meeting, The Combustion Institute, Atlanta GA, March, 2011. 20–23.
[25] W.J. Pitz, N.P. Cernansky, F.L. Dryer, F.N. Egolfopoulos, J.T. Farrell, D.G. Friend, H. Pitsch, SAE 2007-01-0175, 2007.
[26] S. Jerzembeck, N. Peters, Pepiot-Desjardins, H. Pitsch, Combust. Flame 156 (2009) 292–301.
[27] A. Babajimopoulos, G.A. Lavoie, Combust. Sci. Technol. 179 (2007) 2039–2063.

[28] D. Veynante, L. Vervisch, Prog. Energy Combust. Sci. 28 (2002) 193–266.
[29] J.B. Bell, M.S. Day, J.F. Grcar, Proc. Combust. Inst. 29 (2002) 1987–1993.
[30] E.R. Hawkes, J.H. Chen, Combust. Flame 144 (2006) 112–125.
[31] C.M. Lund, A General Computer Program for Calculating Time-Dependent Phenomena Involving One-Dimensional Hydrodynamics, Transport, and Detailed Chemical Kinetics, Report No. UCRL-52504, Lawrence Livermore National Laboratory, 1978.
[32] Y.F. Tham, F. Bisetti, J.Y. Chen, ASME, J. Eng. Gas Turbines Power 130 (2008).
[33] R.J. Kee, G. Dixon-Lewis, J. Warnatz, M.E. Coltrin, J.A. Miller, A Fortran Computer Code Package For The Evaluation Of Gas-Phase Multicomponent Transport Properties, Report No. SAND86-8246, Sandia National Laboratories, 1986.
[34] S.G. Davis, C.K. Law, Combust. Sci. Technol. 140 (1998) 427–449.
[35] K. Kumar, J.E. Freeh, C.J. Sung, Y. Huang, J. Prop. Power 23 (2007) 428–436.
[36] C.K. Westbrook, A.A. Adamczyk, G.A. Lavoie, Combust. Flame 40 (1981) 81–99.
[37] M.M. Andreae, W.K. Cheng, T. Kenney, J. Yang, SAE 2007–01-1858, 2007.